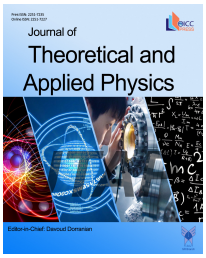

Volume 18, Issue 6, 182476 (1-12)

Journal of Theoretical and Applied Physics (JTAP)

https://dx.doi.org/10.57647/j.jtap.2024.1806.76

Investigation of anomalous Nernst effect in ferromagnetic Weyl semimetal

Udai Prakash Tyagi, Partha Goswami*

D.B.College, University of Delhi, Kalkaji, New Delhi, India.

***Corresponding author:** physicsgoswami@gmail.com

Original Research

Received:
8 September 2024
Revised:
21 October 2024
Accepted:
4 November 2024
Published online:
30 December 2024

Abstract:

In a three-dimensional Dirac semimetal the time reversal symmetry (TRS) or the inversion symmetry (IS) is not broken. With either of these symmetries broken, the Dirac points in the three-dimensional band structure split up into pairs of so-called Weyl points. The ferromagnetic Weyl semimetals (FMWSM), such as $Co_3Sn_2S_2$, feature pairs of Weyl points characterized by the opposite chiralities. In this communication we study FMWSM based on TRS broken continuum and lattice Hamiltonians. The latter one is more realistic and represents $Co_3Sn_2S_2$. These models include all essential ingredients leading to the formation of a pair of Weyl nodes and tilted Weyl cones. Our analysis shows a large anomalous Nernst conductivity which is unlocked due to the divergent Berry curvature-a local manifestation of the geometric properties of electronic wavefunctions-at Weyl points.

Keywords: Ferromagnetic Weyl semimetals; Weyl points of opposite chiralities; Tilted Weyl cone; Berry curvature; Anomalous Nernst conductivity

1. Introduction

The Weyl fermion quasiparticles (WFQPs)are massless and have a definite chirality-a new degree of freedom in the relativistic Hamiltonian describing a quantum mechanical state. For such QPs, the chirality/handedness is determined by the sign of its spin polarization along the momentum direction [1, 2]. One may choose the index $\chi = \pm 1$ to represent two Weyl fermions (WFs) of opposite chiralities, say at wavevectors $+k_0$ and $-k_0$, in a Weyl semimetal (WSM). This host material is such that the time reversal symmetry (TRS) is broken but the parity is preserved. A gauge field that couples differently to WFs in this material with two chiralities is called the chiral gauge field. As a consequence, the chiral charge conservation is violated in a theory of WFQPs, typically in the presence of parallel electric and magnetic fields. The violation is referred to as the chiral anomaly [3]. The WF and the chiral anomaly [4, 5] act as a link between the condensed matter and high-energy physics (HEP). The introduction of the idea was originally motivated by the decay process of neutral pion in the context of HEP [5]. These quasi-particles play a central role in the relativistic field theory. In condensed matter physics (CMP), the central concepts of causality and the allied event horizon in spacetime can be carried over into the field of correlated WSM. This strong association between condensed matter and high-energy physics is thoroughly explored in reference [6].

The Weyl semimetals, e.g., transition mono-pnictides TaAs, TaP, NbP, etc. [7–12], WTe_2 [13], magnetic compounds such as $Co_3Sn_2S_2$ [14–21], Co_2MnGa [22], and so on have been one of the areas of great interest of the CMP community for quite some time. These materials provide the realization of WFQPs-low energy excitations-around the Weyl points. The Weyl nodes (WNs) are the isolated points in the Brillouin zone (BZ) carrying non-trivial chiral charge (chiral charge is equal to the Chern number on a small spherical manifold enclosing the Weyl point in the bulk BZ) where pairs of nondegenerate bands of opposite chirality cross/touch each other linearly or almost linearly. These points are seperated in the momentum space. While a right-handed WN (chirality index $\chi = +1$) is a source, a left-handed one (chirality index $\chi = -1$) is a drain (see Figure 1) in the context of Berry Curvature (BC). It may be mentioned that the presence of WNs is manifested by non-trivial topological properties such as negative magnetore-

sistance ascribed to chiral anomaly and the exotic surface Fermi arcs (SFA). As shown in Figure 1, SFA is an open curve joining the projections of WNs of opposite chiralities in the bulk BZ onto the surface BZ. The chiral charge mentioned above is responsible for the existence of the SFA [23, 24]. More about SFA is discussed in section 5. The non-trivial topology of the WSMs [7–21, 25] is an upshot of the broken time reversal symmetry (TRS) or the space inversion symmetry (SIS) or the both of them with/without strong correlations.

The stability of the Weyl nodes requires the broken symmetry scenario. If TRS and the space inversion symmetry (SIS) are both broken the minimal number of Weyl nodes must be two. This is in agreement with the Nielsen-Ninomiya theorem [26] that requires the number of Weyl points in the Brillouin zone to be even. Quite intriguingly, it has been shown that the ferromagnetic WSM Fe_3Sn_2 [27–29] shows a large, albeit even number of Weyl nodes, close to the Fermi energy. Such host systems have been reported to provide favorable prospect for the emergence of interesting quantum phases/phase transition, such as the Weyl charge density wave (CDW) (standing waves with a periodicity different from the underlying atomic lattice) phase in $(TaSe_4)_2I$ and Mo_3Al_2C [6, 30], the ferromagnetic ground state and the possible nontrivial superconductor state of the alluaudite type compound $K_2Mn_3(AsO_4)_3$ [31], the interesting transition from the normal CDW phase to exotic, strong coupling superconducting state possibly with *s*-wave symmetry in kagome metals AV_3Sb_5 (A=K, Rb, Cs) [32–34], the ferromagnetic Weyl semi-metallic (FMWSM) phase of the transition metal based Kagome compound $Co_3Sn_2S_2$ [14–21], and so on. In fact, in Kagome materials the atoms in a layer form a lattice resembling a traditional Japanese basket-weaving pattern. The study of these materials, including $K_2Mn_3\ (AsO_4)_3$ [31] and the frustated Kagome ferromagnetic alloy Fe_3Sn_2 [27–29], provides an attainable pulpit to probe the intrinsic properties related to Weyl nodes, and the allied device applications. In this paper, however, we theoretically investigate continuum and lattice models of FMWSM, such as the Kagome compound $Co_3Sn_2S_2$ [14–21]. The characteristic feature of FMWSM is a large anomalous Nernst effect (ANE) [35] which is unlocked due to the divergent BC-a local manifestation of the geometric properties of electronic wavefunctions-at Weyl nodes. We obtain the Berry curvature and the anomalous Nernst conductivity within the framework of a continuum model [16, 20, 21] of FMWSM in this communication.

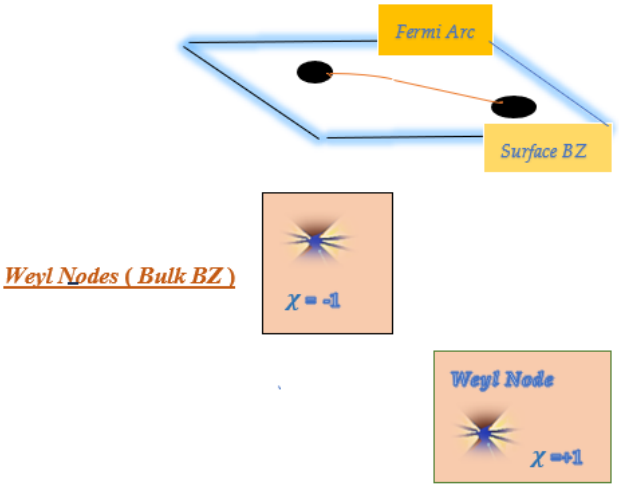

Figure 1. A cartoon of the Weyl nodes (WNs) of different chirality in the bulk Brillouin zone (BZ) and the Fermi arc (FA)in the surface BZ (for the WSM case). The presence of WN is manifested by surface FA that connect the WNs of opposite chirality. The explanation related to the surface FA formation could be found in section 5. The chirality index $\chi = +1(-1)$ corresponds to momentum space pseudo-magnetic monopole(anti-monopole). The former is a source of Berry curvature (BC), while the latter is a drain.

The paper is organized as follows: In section 2, we present a continuum model and the more realistic lattice model [16, 21] of FMWSM bulk. The former includes all essential ingredients leading to the formation of a pair of Weyl nodes and tilted Weyl cones. We obtain the energy eigenspectra and the corresponding eigenvectors of these model Hamiltonians in section 3. In section 4, we present our findings on the topological properties appearing in the continuum model in the section 2. The paper ends with discussion, future perspectives, and conclusion in section 5.

2. Model Hamiltonians

2.1 High symmetry points

The Weyl fermion quasiparticles in a Weyl semimetal (WSM) are very robust. Except the translation symmetry of the crystal lattice, these fermions do not depend on other symmetries. These fermions possess a high degree of mobility. As regards FMWSM, the representative compound $Co_3Sn_2S_2$ is a ferromagnet with a Curie temperature of $T_c \sim 180$ K. The structure is composed of triangular Sn and S layers interspersed between the Kagome lattice planes of Co atoms. These Co atoms are responsible for ferromagnetic order. Ozawa et al. have analysed a momentum-space model Hamiltonian [16, 21, 35] of $Co_3Sn_2S_2$ and the corresponding electronic band structure. This two-orbital archetypal model [16, 21] represents FMWSM $Co_3Sn_2S_2$ with great details with the effective Kane-Mele type spin-orbit coupling (SOC) [36] between the Co atoms in the Kagome plane. The unit cell includes three Co atoms on the Kagome lattice and one Sn atom on the triangular lattice. The model is described by a primitive lattice with three basis vectors: $\mathbf{a}_1$, $\mathbf{a}_2$, and $\mathbf{a}_3$ where $\mathbf{a}_1 = a(1/2,\ 0,\ c/a)$, $\mathbf{a}_2 = a(-1/4,\ \sqrt{3}/4,\ c/a)$ and $\mathbf{a}_3 = a(-1/4,\ -\sqrt{3}/4,\ c/a)$. In the case of bulk $Co_3Sn_2S_2$ the lattice parameters are 5.37 *Å* and 13.17 *Å* along (a, b) and c directions, respectively. The lattice parameters a, b, and c are measured by single crystal diffraction to be 5.3657 *Å*, 5.3657 *Å* and 13.1710 *Å*, respectively. While he angle $\alpha = 59.91647°$ (58.33°), the angle between a and b is $\gamma = 118.78°$. The intralayer lattice vectors of a Kagome layer $(\mathbf{b}_1, \mathbf{b}_2, \mathbf{b}_3)$ (the first-nearest-neighbour vectors), $(\mathbf{d}_1, \mathbf{d}_2, \mathbf{d}_3)$ (the second-nearest-neighbour vectors), and the interlayer lattice vectors of Kagome layers $(\mathbf{c}_1, \mathbf{c}_2, \mathbf{c}_3)$ (the first-nearest-neighbour vectors) were represented

in Ref. [16, 21, 35] in a certain way. In this communication, we, however, choose to write

$$\begin{aligned}\mathbf{a}_1 &= a(\cos\frac{\gamma}{2}, 0, \frac{c}{a}),\\ \mathbf{a}_2 &= a(-\frac{1}{2}\cos\frac{\gamma}{2}, \frac{\sqrt{3}}{2}\cos\frac{\gamma}{2}, \frac{c}{a}),\\ \mathbf{a}_3 &= a(-\frac{1}{2}\cos\frac{\gamma}{2}, -\frac{\sqrt{3}}{2}\cos\frac{\gamma}{2}, \frac{c}{a}),\end{aligned} \tag{1}$$

where the interaxial angle γ is that between $\mathbf{a}_1$ and $\mathbf{a}_2$. The lattice vectors ($\mathbf{b}_1$, $\mathbf{b}_2$, $\mathbf{b}_3$), ($\mathbf{d}_1$, $\mathbf{d}_2$, $\mathbf{d}_3$), and ($\mathbf{c}_1$, $\mathbf{c}_2$, $\mathbf{c}_3$) are expressed in terms of the angle γ as shown below

$$\begin{aligned}\mathbf{b}_1 &= \frac{\mathbf{a}_2-\mathbf{a}_1}{2} = \frac{a}{2}(-\frac{3}{2}\cos\frac{\gamma}{2}, \frac{\sqrt{3}}{2}\cos\frac{\gamma}{2}, 0),\\ \mathbf{b}_2 &= \frac{\mathbf{a}_3-\mathbf{a}_2}{2} = \frac{a}{2}(0, -\sqrt{3}\cos\frac{\gamma}{2}, 0),\\ \mathbf{b}_3 &= \frac{\mathbf{a}_1-\mathbf{a}_3}{2} = \frac{a}{2}(\frac{3}{2}\cos\frac{\gamma}{2}, \frac{\sqrt{3}}{2}\cos\frac{\gamma}{2}, 0),\end{aligned} \tag{2}$$

$$\begin{aligned}\mathbf{d}_1 &= \mathbf{b}_3-\mathbf{b}_2 = \frac{a}{2}(\frac{3}{2}\cos\frac{\gamma}{2}, \frac{3\sqrt{3}}{2}\cos\frac{\gamma}{2}, 0),\\ \mathbf{d}_2 &= \mathbf{b}_1-\mathbf{b}_3 = \frac{a}{2}(-3\cos\frac{\gamma}{2}, 0, 0),\\ \mathbf{d}_3 &= \mathbf{b}_2-\mathbf{b}_1 = \frac{a}{2}(\frac{3}{2}\cos\frac{\gamma}{2}, \frac{-3\sqrt{3}}{2}\cos\frac{\gamma}{2}, 0),\end{aligned} \tag{3}$$

$$\begin{aligned}\mathbf{c}_1 &= \frac{\mathbf{a}_1+\mathbf{a}_2}{2} = \frac{a}{2}(\frac{1}{2}\cos\frac{\gamma}{2}, \frac{\sqrt{3}}{2}\cos\frac{\gamma}{2}, 2\frac{c}{a}),\\ \mathbf{c}_2 &= \frac{\mathbf{a}_2+\mathbf{a}_3}{2} = \frac{a}{2}(-\cos\frac{\gamma}{2}, 0, 2\frac{c}{a}),\\ \mathbf{c}_3 &= \frac{\mathbf{a}_3+\mathbf{a}_1}{2} = \frac{a}{2}(\frac{1}{2}\cos\frac{\gamma}{2}, -\frac{\sqrt{3}}{2}\cos\frac{\gamma}{2}, 2\frac{c}{a}).\end{aligned} \tag{4}$$

The reciprocal space is very useful as it provides a natural language for describing periodic systems and all periodic responses are contained within the first Brillouin zone (BZ). The reciprocal lattice vectors ($\boldsymbol{\rho}_1(\gamma), \boldsymbol{\rho}_2(\gamma), \boldsymbol{\rho}_3(\gamma)$) in terms of the angle γ are given by $a\boldsymbol{\rho}_1(\gamma)/2\pi = (4\sqrt{3}\zeta,\ 2\zeta,\ 3\xi)$, $a\boldsymbol{\rho}_2(\gamma)/2\pi = (-2\sqrt{3}\zeta,\ 6\zeta,\ 2\xi)$, and $a\boldsymbol{\rho}_3(\gamma)/2\pi = (-2\sqrt{3}\zeta,\ -8\zeta,\ 2\xi)$, where $\zeta \equiv \frac{1}{7\sqrt{3}}\sec(\gamma/2)$,and $\xi = a/7c$. By using these reciprocal vectors, it is easy to translate the lattice points in reciprocal space and build the corresponding reciprocal lattice for the prototypical kagome magnetic WSM under consideration. The high-symmetry points (HSPs) in the reciprocal space are important for describing the electronic and magnetic properties of solids. Upon using the frame-work outlined in Ref. [16, 21], the coordinates of high symmetry k-points have been obtainted here. The relevant HSPs, viz. T, L, U, and W points are given by $(2\pi/a)$ $(0,\ 0,\ 7\xi/2)$, $(2\pi/a)$ $(2\sqrt{3}\zeta,\ \zeta,\ 3\xi/2)$, $(2\pi/a)$ $(\eta,\ 0,\ 7\xi/2)$, and $(2\pi/a)$ $(-\eta,\ \eta/\sqrt{3},\ 7\xi/2)$ respectively, where $\eta \equiv 2\sqrt{3}\zeta - (\sqrt{3}\xi^2)/(2\xi)$. We calculate the coordinates of HSPs, setting the value of c/a and $\gamma = 118.78°$. We obtain T, L, U, and W points as $(2\pi/a)$ $(0,\ 0,\ 0.2037)$, $(2\pi/a)$ $(0.5611,\ 0.1620,\ 0.0873)$, $(2\pi/a)$ $(0.5430,\ 0,\ 0.2037)$, and $(2\pi/a)$ $(-0.5430,\ 0.3135,\ 0.2037)$, respectively. We use these results below in graphical representation of the single particle excitation spectrum. Here one needs to keep in mind that, depending on the conventions used for defining the reciprocal lattice vectors and the choice of the primitive cell, there may be some differences in the exact coordinates of high-symmetry points reported in different references or databases. However, the relative positions of the high-symmetry points and their symmetry properties should be consistent among different descriptions.

2.2 Continuum model

The Hamiltonian of a general 2-level system can always be written in the basis of the three Pauli matrices ($\boldsymbol{\sigma}$). We now present an extended version of the continuum model of WSM in Refs. [20] in the basis of these matrices. This is given by

$$\begin{aligned}\acute{H}_\xi(\mathbf{k}) =& \xi\hbar v_F a^{-1}\mathbf{k}\cdot\boldsymbol{\sigma} + (\xi\hbar a^{-1}\boldsymbol{\beta}_{\boldsymbol{\xi}}\cdot\mathbf{k} - \mu)\sigma_0 + P(\mathbf{k})\sigma_z -\\ & \xi Q\sigma_z + \mathbf{M}(\eta_1, \eta_2, \theta)\cdot\boldsymbol{\sigma},\end{aligned} \tag{5}$$

where $P(\mathbf{k}) = P_0 - P_1(k_x^2 + k_y^2) - P_1k_z^2$ with $\mathbf{K} = a(k_x,\ k_y,\ (c/a)k_z)$, $(P_0,\ P_1)$ are the relevant material dependent parameters in units of energy, and μ is the chemical potential of the fermion number. While $\xi = \pm 1$ specifies the chirality of the Weyl points, the energy parameter Q determines the shift of the Weyl nodes. The Pauli matrices $\boldsymbol{\sigma}$ are acting in the space of bands that make contact at Weyl point pairs. We take the Fermi velocity v_F to be positive. We have included the magnetic moment (clubbed with the exchange field) $\mathbf{M}(\eta_1,\ \eta_2,\ \theta)$ in order to take care of the ferromagnetic order. The time reversal (TR) operator for a spin 1/2 particle is $\Theta = -i\sigma_y K$. The operator K stands for the complex conjugation. We find that $\Theta\acute{H}_\xi(\mathbf{k})\Theta^{-1} \neq \acute{H}_\xi(-\mathbf{k})$, i.e. the time reversal symmetry (TRS) is not obeyed. We shall on focus on neighborhood of HSPs T, L, U, and W for graphical representations. For T and U, in particular, $ak_y = 0$, while for L and W we have $ak_y = ak_{y0} = 0.1620$ and 0.3135 respectively. Thus, one can then think of the Hamiltonian involving the wave vector components $(ak_{(z,x)}, 0/ak_{y0})$ as an effective two-dimensional Hamiltonian in momentum space for the investigation purpose. The magnetic moment, in general, may be given by $\mathbf{M} = M(\sin\psi\cos\varphi,\ \sin\psi\sin\varphi,\ \cos\psi)$ in spherical polar coordinates. However, we assume that the spin structure depends on the angle θ formed by the spin moments and the y-axis perpendicular to the $z-x$ plane of the sample with length, breadth, and width along $z-$, $x-$, and $y-$axes, respectively. In that case, one may write $\mathbf{M}(\eta_1,\ \eta_2,\ \theta) = M(\eta_1\sin\theta,\ \eta_2\sin\theta,\ \cos\theta)$, where $\eta_1^2 + \eta_2^2 = 1$. While $\theta = 0$ corresponds to the ferromagnetic order along the axis perpendicular to the $z-x$ plane, $\theta = 90°$ corresponds to the in-plane spin order. Apart from the former case, our focus will also be on the latter case. The reason being the FM materials with in-plane magnetization has not been studied so extensively compared to those with the out of the plane magnetization. The tilt of the Weyl cones is described by the parameters $\boldsymbol{\beta}_{\boldsymbol{\xi}}$ - the tilt velocity. We shall mainly focus on the case $\boldsymbol{\beta}_{\boldsymbol{\xi}} = \beta_\xi\mathbf{e}$, where the unit vector $\mathbf{e}$ is assumed to be in the $x-z$ plane. Therefore, one may write $\mathbf{e} = (\cos\psi,\ 0,\ \sin\psi$. It must be noted here the strain can modify a pre-existing tilt making it

inhomogeneous through the sample. Upon dividing both the sides of Eq. (1) by $(\hbar v_F a^{-1})$, one obtains the dimensionless Hamiltonian

$$H_\xi(\mathbf{k},Q) = \xi v_F a^{-1}(\mathbf{k}-\xi e\mathbf{A})\cdot\boldsymbol{\sigma} + (\xi v_F a^{-1}\boldsymbol{\alpha_\xi}\cdot\mathbf{k}-\mu)\sigma_0 + P(\mathbf{k})\sigma_z - \xi Q\sigma_z \quad (6)$$

where $\hbar = 1$, $\mathbf{A} = -(\mathbf{M}(\eta_1,\ \eta_2,\ \theta))/(ev_F a^{-1})$,and $\boldsymbol{\alpha_\xi} = \boldsymbol{\beta}/v_F$. The parameter $\boldsymbol{\alpha_\xi}$ is the dimensionless tilt velocity. Obviously enough, the magnetic moments in our general structure is equivalent to the chiral gauge field $\mathbf{A}$. Furthermore, one can write the second term $(\xi\boldsymbol{\alpha_\xi}\cdot\mathbf{k}\sigma_0)$ as $(\xi\boldsymbol{\alpha_\xi}\mathbf{e}\cdot\mathbf{k}\sigma_0)$. We notice that, in the absence of the tilt, the Hamiltonian obeys $PH_\xi(\mathbf{k})P^{-1} = -H_\xi(-\mathbf{k})$ where the particle-hole symmetry (PHS) operator $P = \sigma_x K$. Thus, the tilt factor breaks PHS. Whereas for the type-I WSM the tilt factor $|\alpha_\xi| < 1$, for the type-II variety it is greater than one. We present the investigation of the model Hamiltonian (2) in section 3. The investigation may serve as a platform for realizing large anomalous Nernst effect.

2.3 Lattice model

In the kagome compound $Co_3Sn_2S_2$, an important feature is that the p orbitals of post-transition metal (Sn) atoms overlap and hybridize with the transition metal (Co) $3d$ orbitals near the Fermi level. In fact, the states at the Fermi level are comprised primarily of Co-$3d$ orbitals. Therefore, an archetypal Hamiltonian for the compound $Co_3Sn_2S_2$ must involve the $p-d$ hybridization. Also, there have to be a term representing ferromagnetism of Co atoms, and the Kane-Mele type spin-orbit coupling ($t_{\rm soc}$) involving the second-nearest-neighbour intralayer lattice vectors of a Kagome layer ($\mathbf{d}_1$, $\mathbf{d}_2$, $\mathbf{d}_3$); this term is zero when for the first neighbor (the lattice vectors are ($\mathbf{b}_1$, $\mathbf{b}_2$, $\mathbf{b}_3$)) is involved. The origin of this term can be traced back to the Sn atom residing on the center of each hexagon in the kagome lattice. Furthermore, there are the hopping integrals, viz. the first-neighbor hopping (t_1) and the second-neighbour hopping (t_2) in the Kagome layer. It must be mentioned that NN and NNN hopping terms, which describe the interactions between Co atoms in the Kagome lattice plane, were found to be inadequate for capturing the nodal line feature [16, 21]. Therefore, the inter-Kagome-layer hopping (t_z) needs to be included. Upon introducing the term ($M\sigma_z$) describing the ferromagnetic ordering within the mean field approximation, the onsite energy of p orbital and d orbitals, (ε_p, ε_d), and the hopping integral (t_{pd}) between nearest Co and Sn1 sites, the momentum space representation of the Hamiltonian, in the basis $(d_{k.A,\tau=\uparrow,\downarrow} d_{k,B,\tau} d_{k,C,\tau} p_{k\cdot\tau})^T$ where $d_{k.A,\tau}$ and $p_{k\cdot\tau}$, respectively, are the destruction operators corresponding to $d-$ and $p-$electrons, τ is the spin index and the (A, B, C) are sub-lattice indices, is expressed as $\Im = \Im_1 + \Im_2$. Here

$$\Im_1 = M\begin{pmatrix}\sigma^{12} & \mathbf{0}\\ \mathbf{0} & \frac{1}{2}(\sigma^{12}+\gamma^3\gamma^5)\end{pmatrix} + \varepsilon\begin{pmatrix}\Pi & \mathbf{0}\\ \mathbf{0} & \frac{1}{2}(\Pi+\gamma^0)\end{pmatrix} + (\varepsilon_p-\mu)\begin{pmatrix}0 & \mathbf{0}\\ \mathbf{0} & \frac{1}{2}(\Pi+\gamma^0)\end{pmatrix},$$

$$\begin{aligned}\Im_2 = {}& \acute{\mathrm{A}}_1\begin{pmatrix}\gamma^5 & \mathbf{0}\\ 0 & \mathbf{0}\end{pmatrix} + i\acute{\acute{\mathrm{A}}}_1\begin{pmatrix}\gamma^3 & \mathbf{0}\\ 0 & \mathbf{0}\end{pmatrix} + \\ & \acute{\mathrm{A}}_2\begin{pmatrix}\mathbf{0} & \frac{1}{2}(\Pi+\gamma^0)\\ \frac{1}{2}(\Pi+\gamma^0) & 0\end{pmatrix} - \\ & i\acute{\acute{\mathrm{A}}}_2\begin{pmatrix}\mathbf{0} & \frac{1}{2}(\sigma^{12}+\gamma^3\gamma^5)\\ -\frac{1}{2}(\sigma^{12}+\gamma^3\gamma^5) & 0\end{pmatrix} + \\ & \acute{\mathrm{A}}_3\begin{pmatrix}\mathbf{0} & \frac{1}{2}(\gamma^5-\gamma^0\gamma^5)\\ \frac{1}{2}(\gamma^5+\gamma^0\gamma^5) & 0\end{pmatrix} - \\ & i\acute{\acute{\mathrm{A}}}_3\begin{pmatrix}\mathbf{0} & \frac{1}{2}(\gamma^3-\gamma^0\gamma^3)\\ \frac{1}{2}(\gamma^3+\gamma^0\gamma^3) & 0\end{pmatrix} + \\ & \mathbf{B}_1\begin{pmatrix}\mathbf{0} & \frac{1}{2}(\gamma^5+\gamma^0\gamma^5)\\ \frac{1}{2}(\gamma^5-\gamma^0\gamma^5) & 0\end{pmatrix} + \\ & \mathbf{B}_2\begin{pmatrix}\mathbf{0} & \frac{1}{2}(\Pi-\gamma^0)\\ \frac{1}{2}(-\Pi+\gamma^0) & 0\end{pmatrix} + \\ & \mathbf{B}_3\begin{pmatrix}\mathbf{0} & 0\\ 0 & \gamma^0\gamma^5\end{pmatrix}\end{aligned} \quad (7)$$

Here Π is the 4×4 identity matrix, $\sigma^{\nu\rho} = (i/2)[\gamma_\nu,\ \gamma_\rho]$, and the anti-commuting $(1/2\{\gamma^\mu,\ \gamma^\nu\} = g^{\mu\nu}\Pi)$ matrices $(\gamma^0,\ \gamma^1,\ \gamma^2,\ \gamma^3,\ \gamma^5)$ are Dirac matrices in contravariant notations. We note that the γ^0 matrix is hermitian while the $(\gamma^1,\ \gamma^2,\ \gamma^3)$ matrices are anti-hermitian. Furthermore,

$$\begin{aligned}\acute{\mathrm{A}}_1 &= 2t_1\cos(\mathbf{b}_1,\mathbf{k}) + 2t_2\cos(\mathbf{d}_1,\mathbf{k}) + 2t_z\cos(\mathbf{c}_1,\mathbf{k}),\\ \acute{\acute{\mathrm{A}}}_1 &= 2t_{soc}\cos(\mathbf{d}_1,\mathbf{k}),\end{aligned} \quad (8)$$

$$\begin{aligned}\acute{\mathrm{A}}_2 &= 2t_1\cos(\mathbf{b}_3,\mathbf{k}) + 2t_2\cos(\mathbf{d}_3,\mathbf{k}) + 2t_z\cos(\mathbf{c}_3,\mathbf{k}),\\ \acute{\acute{\mathrm{A}}}_2 &= 2t_{soc}\cos(\mathbf{d}_3,\mathbf{k}),\end{aligned} \quad (9)$$

$$\begin{aligned}\acute{\mathrm{A}}_3 &= 2t_1\cos(\mathbf{b}_2,\mathbf{k}) + 2t_2\cos(\mathbf{d}_2,\mathbf{k}) + 2t_z\cos(\mathbf{c}_2,\mathbf{k}),\\ \acute{\acute{\mathrm{A}}}_3 &= 2t_{soc}\cos(\mathbf{d}_2,\mathbf{k}),\end{aligned} \quad (10)$$

$$\begin{aligned}\mathbf{B}_1 &= 2it_{pd}\sigma_0\sin(\frac{1}{2}\mathbf{a}_1,\mathbf{k}),\\ \mathbf{B}_2 &= 2it_{pd}\sigma_0\sin(\frac{1}{2}\mathbf{a}_2,\mathbf{k}),\\ \mathbf{B}_3 &= 2it_{pd}\sigma_0\sin(\frac{1}{2}\mathbf{a}_3,\mathbf{k}),\end{aligned} \quad (11)$$

where $\varepsilon = (\varepsilon_d - \mu)$. Thus, $\Im$ is a 8×8 matrix. Here $\acute{\sigma}_j s$ are the Pauli matrices and μ is the chemical potential of the fermion number. The model is described by a primitive lattice with three basis vectors: $\mathbf{a}_1$, $\mathbf{a}_2$, and $\mathbf{a}_3$ given above. In this model, the unit cell includes three Co atoms on the kagome lattice and one Sn atom on the triangular lattice, as already mentioned.

3. Energy eigenspectra

The energy eigenvalues ($E_{\alpha,\xi}$, $\alpha = \pm1$) of the matrix (5) for $\mu = 0$ are given by (Appendix A)

$$E_{\alpha,\xi} = \alpha\Big((P(\mathbf{k}) + \xi\hbar v_F\frac{c}{a}k_z + M\cos\theta - \xi Q)^2 + \hbar^2 v_F^2 a^{-2}(a^2k_x^2 + a^2k_y^2) + M_1^2\Big)^{\frac{1}{2}}, \quad (12)$$

where $M_1^2 \equiv M^2 \sin^2\theta + 2\hbar v_F a^{-1}\xi M \sin\theta(\eta_1 ak_x + \eta_2 ak_y)$. Here the tilt parameter $\boldsymbol{\beta}_\xi = 0$. The 2D plots of the energy eigenvalues (of the Hamiltonian matrix in (1)) as a function of ck_z are shown in Figure 2. In Fig. 2(a) $ak_x = 0.5611$, and $ak_y = 0.1620$. In Fig. 2(b) $ak_x = -0.5430$, and $ak_y = 0.3135$. The numerical values of the other parameters used are $P_0 = 0.32$, $P_1 = 2.71$, $M = 1$, $\mu = 0$, $Q = 0.8$, $v/a(v = v_F) = 0.26$, $\theta = 0$, $\eta_1 = 0$ and $\eta_2 = 1$. The angle $\theta = 0$ corresponds to the ferromagnetic order along the $z-$direction. The dimensionless momentum parameter $\xi = Q/\hbar v_F a^{-1}$ determines the shift of the Weyl nodes. The bands of opposite chirality almost linearly touch each other at WNs. The vertical (horizontal) lines indicate avoided crossing momenta (the fermi energy $E_F = 0$). The Figures 2(c), and (d) correspond to the in-plane spin ordering as $\theta = \pi/2$. The rest of the parameter values in these figures are the same as in Figures 2(a), and (b). In the two Figures 2(c), and (d), the chemical potential lies within the band gap, i.e., the system is in the insulating state. However, since the chiral gauge field $\mathbf{A} = -\mathbf{M}(\eta_1, \eta_2, \theta)/ev_F a^{-1} \neq 0$ the time reversal symmetry (TRS) is not preserved by Eq. (5). This leads to non-zero Berry curvature (BC). If one is able to show that the system in this case has access to the integer values of the chern number (C), one can conclude that the system is in the anomalous quantum Hall insulating state. This exercise will be taken up in section 4.

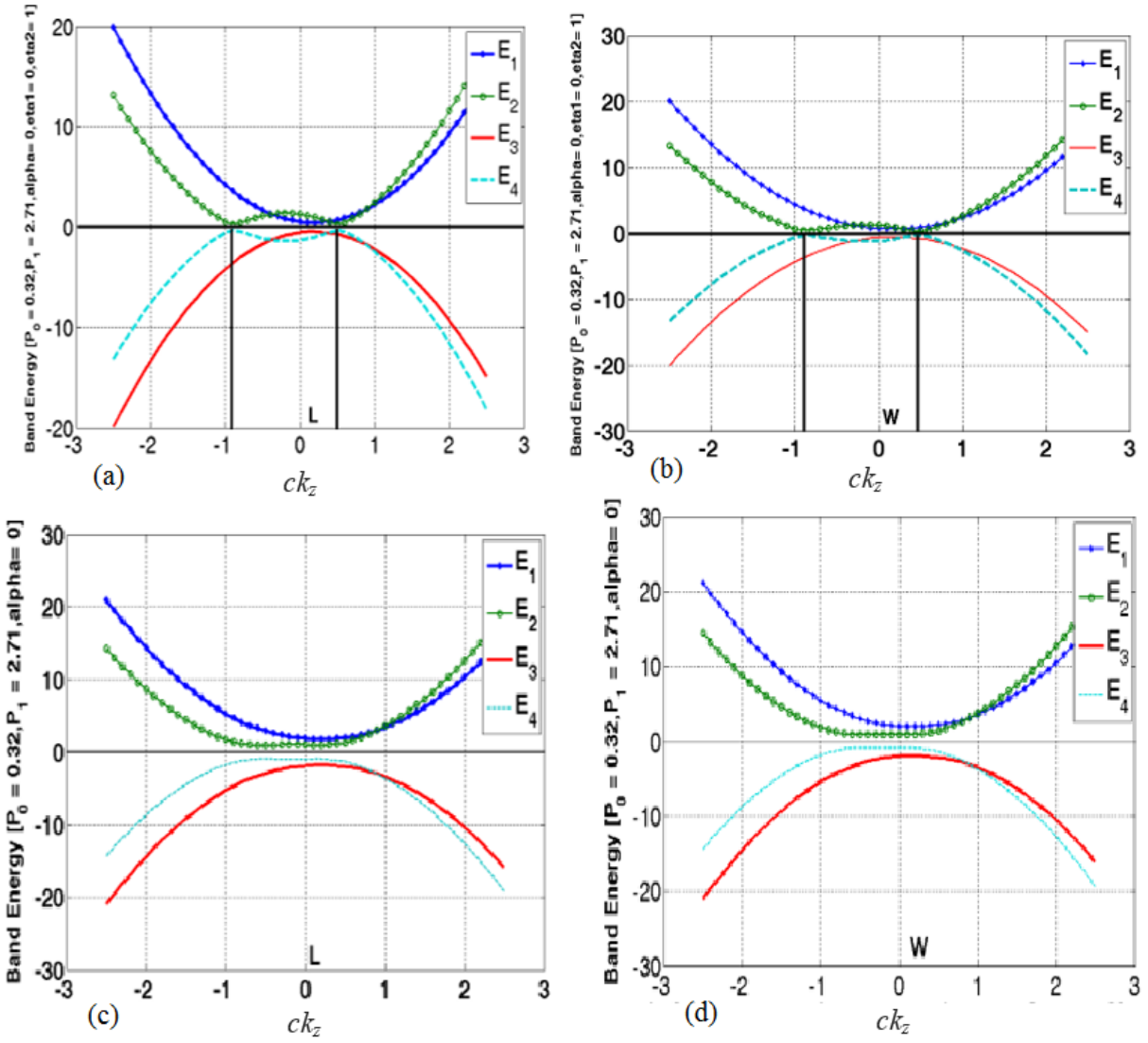

Figure 2. Plots of the energy eigenvalues (of the Hamiltonian matrix in (5)) as a function of ck_z (the tilt parameter $\beta_\xi = 0$) around the HSPs L and W. In (a) and (c) $ak_x = 0.5611$, and $ak_y = 0.1620$. In (b) and (d) $ak_x = -0.5430$, and $ak_y = 0.3135$. (a) and (b) The numerical values of the other parameters used are $P_0 = 0.32$, $P_1 = 2.71$, $M = 1$, $\mu = 0$, $Q = 0.8$, $v/a(v = v_F) = 0.26$, $\theta = 0$, $\eta_1 = 0$, and $\eta_2 = 1$. The bands of opposite chirality almost linearly touch each other at WNs. The angle $\theta = 0$ corresponds to the ferromagnetic order along the $z-$direction. The dimensionless momentum parameter $\xi = Q/\hbar v_F a^{-1}$ determines the shift of the Weyl nodes. The vertical (horizontal) lines indicate avoided crossing momenta (the fermi energy $E_F = 0$). The Figures 2(c), and (d) correspond to the in-plane spin ordering as $\theta = \pi/2$. The rest of the parameter values in these figures are the same as in Figures 2(a), and (b). In 2(c) and 2(d), the chemical potential lies within the band gap.

We now consider the case of the non-zero tilt parameter ($|\alpha_\xi| \neq 0$). The energy eigenvalues of (6) are given by

$$E_{\alpha,\xi} = \Upsilon(k) + \alpha[(P(\mathbf{k}) + M\cos\theta + \xi\hbar v_F \frac{c}{a} ak_z - \xi Q)^2 + v_F a^{-2}(a^2k_x^2 + a^2k_y^2) + M_1^2]^{\frac{1}{2}}, \tag{13}$$

where $\alpha = \pm 1$, $\Upsilon(k) \equiv v_F a^{-1}|\alpha_\xi|(ak_x\cos\psi + ck_z\sin\psi)$ and $M_1^2 \equiv M^2\sin^2\theta + 2\hbar v_F a^{-1}\xi M\sin\theta \times (\eta_1 ak_x + \eta_2 ak_y)$. The corresponding eigenvectors are given in Appendix A 5.These will be required while calculating the anomalous Nernst conductivity $\boldsymbol{\alpha_{xy}}$.

The 2D plots of energy eigenvalues in (12) as a function of ck_z are shown in Figure 3. Here, the tilt parameter $|\alpha_\xi| = 0.8$ (Figures 3(a), and (c)) and $|\alpha_\xi| = 2.8$ (Figures 3(b), and (d)). The former corresponds to type-I and the latter to type-II semimetal. In (a) and (b) $ak_x = 0.5611$, and $ak_y = 0.1620$. In (c) and (d) $ak_x = -0.5430$, and $ak_y = 0.3135$. The numerical values of the other parameters used are $P_0 = 0.32$, $P_1 = 2.71$, $M = 1$, $\mu = 0$, $Q = 0.86$, $\theta = 0$, v/a $(v = v_F) = 0.50$, $\eta_1 = 0$, and $\eta_2 = 1$. We have thus shown that, for the FM order along the axis perpendicular to the plane of the system, the bands of opposite chirality almost linearly cross each other with band inversion at Weyl points above and below the Fermi level.

In order to obtain the eigenvalues of the matrix $\Im = \Im_1 + \Im_2$ in Eq. (7) we needed to lean on numerical analysis. Here, we choose a $k_(j)$-path including high symmetry point(s). For the graphical representations, the following numerical values of the various parameters were used: $t_1 = -1$, $t_2 = 0.6t_1$, $t_z = -1.0t_1$, $t_{pd} = 1.80t_1$, $\varepsilon_d = 2.44t_1$, $\varepsilon_p = 3.5t_1$, $\mu = 0$, and $M = 2.0t_1$. We assign the above-mentioned numerical values to the parameters appearing in the expressions ($\acute{A}_1$, $\acute{A}_2$, $\acute{A}_3$, B_1, B_2, $B_3, \cdots$) in Eqs. (7) to (11). We use the 'Matlab' package for this purpose. Upon using the command $[V, D] = eig(\Im_1 + \Im_2)$ the numerical values of the eigenenergy and the corresponding eigenvectors are obtained. The command returns diagonal matrix D of eigenvalues and matrix V whose columns are the corre-

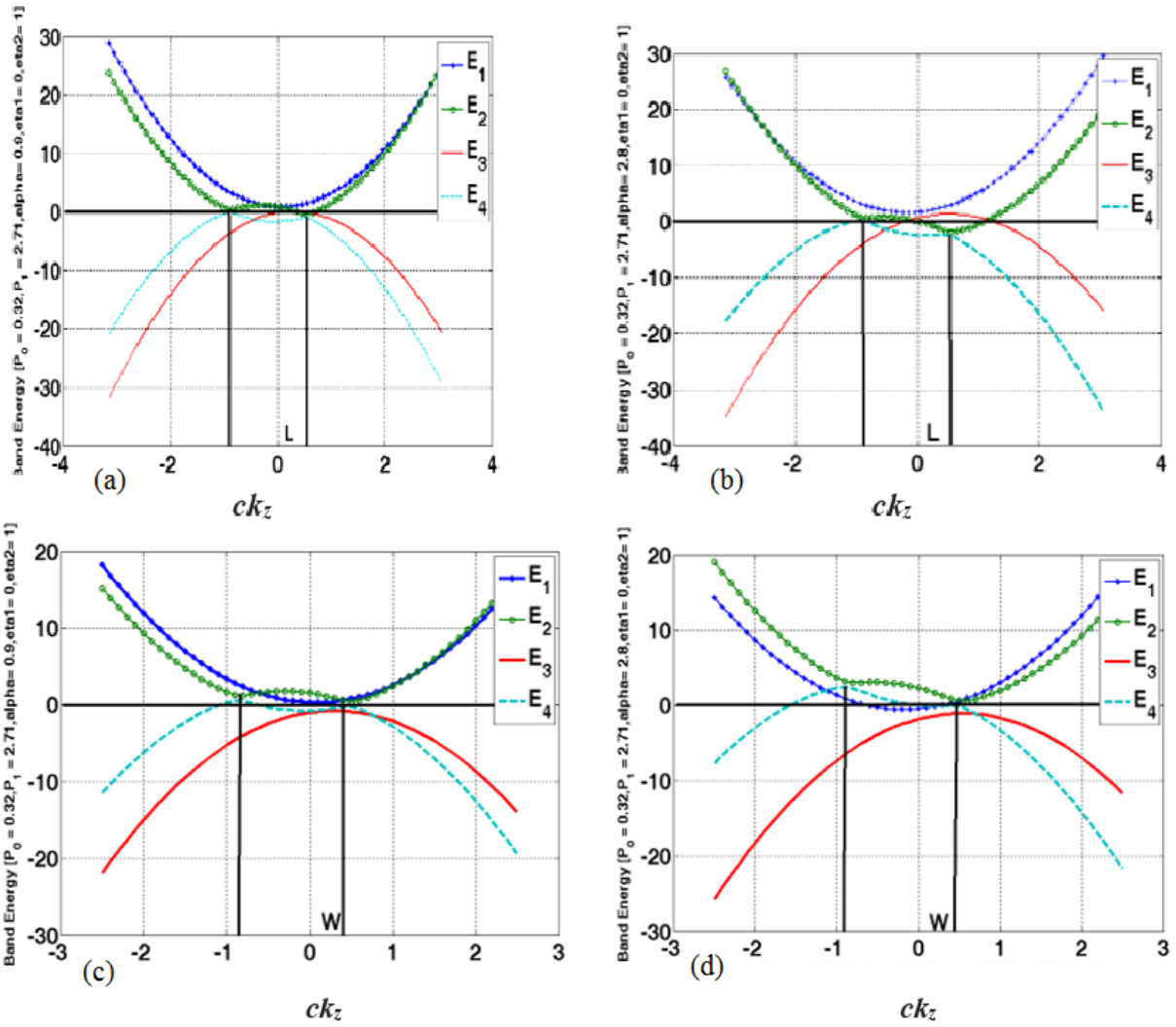

Figure 3. The 2D plots of energy eigenvalues in (12) as a function of ck_z (around the HSPs L and W) are shown in this figure for the tilt parameter $|\alpha_\xi| = 0.9$ (Figures (a) and (c)) and $|\alpha_\xi| = 2.8$ (Figures (b) and (d)). In (a) and (b) $ak_x = 0.5611$, and $ak_y = 0.1620$. In (c) and (d) $ak_x = -0.5430$, and $ak_y = 0.3135$. The numerical values of the other parameters used are $P_0 = 0.32$, $P_1 = 2.71$, $M = 1$, $\mu = 0$, $Q = 0.86$, $\theta = 0$, $v/a(v = v_F) = 0.50$, $\eta_1 = 0$, and $\eta_2 = 1$.

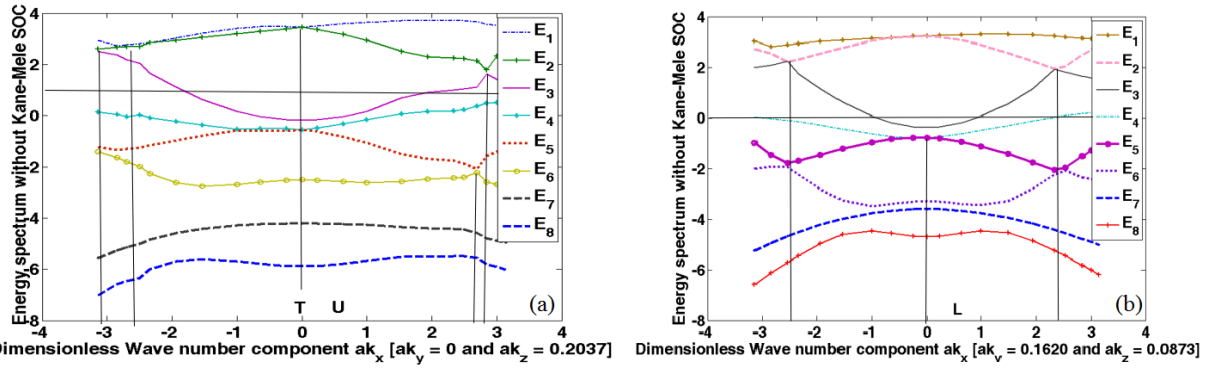

Figure 4. Plots of the energy eigenvalues $E_j(k)$ ($j = 1, 2, \cdots, 8$) corresponding to the matrix $\Im = \Im_1 + \Im_2$ in Eq. (4) as a function of ak_x for (a)($ak_y = 0$, $ck_z = 0, 2037$) and (b)($ak_y = 0.1620$,$ck_z = 0, 0873$). We assume the following numerical values of the various parameters: $t_1 = 1$, $t_2 = 0.6t_1$, $t_z = -1.0t_1$, $t_{pd} = 1.80t_1$, $\varepsilon_d = 2.44t_1$, $\varepsilon_p = 3.5t_1$, $\mu = 0$, $t_{soc} = 0$, and $M = 2.0t_1$. The vertical (horizontal) lines indicate avoided crossing momenta (the fermi energy $E_F = 0$).

sponding right eigenvectors, so that $\Im * V = V * D$. For each $k-$point, in the chosen $k_(j)$-path, this process is repeated. In Figure 4, the plots of the energy eigenvalues $E_j(k)$ ($j = 1, 2, \cdots, 8$) as a function of ak_x, obtained in this manner, are shown for $(\mathbf{a})(ak_y = 0,\ ck_z = 0,\ 2037)$ and $(\mathbf{b})(ak_y = 0.1620,\ ck_z = 0.0873)$ without the Kane-Mele type spin-orbit coupling (SOC). The plots show the Weyl points and the band inversion. The vertical (horizontal) lines indicate avoided crossing momenta (the fermi energy $E_F = 0$). When $t_{soc} \neq 0$ ($|t_{soc}| = 1.80$) the anticrossing feature is present with opening of spectral gaps at some points in the first Brillouin zone (BZ) around L point (see Figure 5). It must be noted that, as shown in the refs [16, 21], there is emergence of the nodal lines centred at the L point of BZ. The investigation of this model is presented very briefly here, as in the subsequent sections our focus will be on the continuum model given by (2). A systematic derivation of the quantities related to Berry curvature (BC) (based on this realistic model), such as the longitudinal magnetoconductivity, and the magneto-thermal conductivity is left for future investigation.

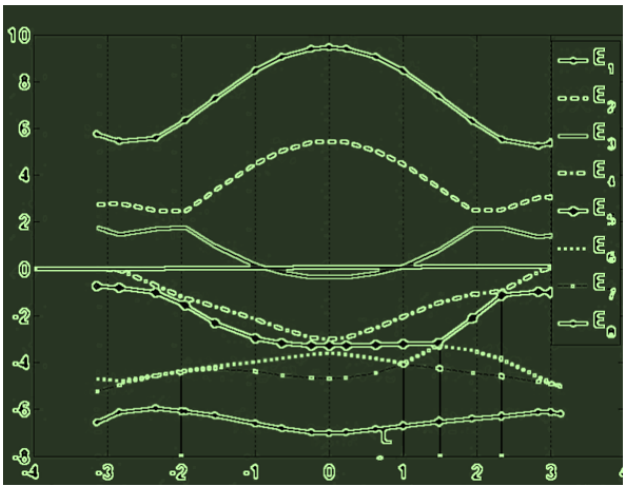

Figure 5. Plots of the energy eigenvalues $E_j(k)$ ($j = 1, 2, \cdots, 8$) corresponding to the matrix $\Im = \Im_1 + \Im_2$ in Eq. (4) as a function of ak_x for ($ak_y = 0.1620$, $ck_z = 0, 0873$). While the wavevector component ak_x is plotted along $x-$axis, the energy eigenvalues are plotted along $y-$axis. We assume the following numerical values of the various parameters: $t_1 = -1$, $t_2 = 0.6t_1$, $t_z = -1.0t_1$, $t_{pd} = 1.80t_1$, $\varepsilon_d = 2.44t_1$, $\varepsilon_p = 3.5t_1$, $\mu = 0$, $|t_{soc}| = 1.80$, and $M = 2.0t_1$.

4. Topological properties

The anomalous Hall effect (AHE) and anomalous Nernst effect (ANE) are critical probes for uncovering the topological properties of charge carriers in magnetic Weyl semimetals (MWSM), as they are primarily driven by the intrinsic magnetic field. In this section, we present our findings on the topological properties appearing in the continuum model in (5). One of the routes to investigate the topological properties is to calculate the Berry curvature (BC), and the anomalous Nernst conductivity (α_{xy}). The chern number (C) quantization related intrinsic Hall conductivity (σ_{xy}) makes no sense for $\theta = 0$ as there is no Chern number in systems which are not gapped. We use the following formula [37, 38] for calculating BC: $\Omega_{xy}^{(n)}(k) = \sum_{\xi, m\neq n} f_{m,n,\xi,\alpha}(k, Q)$, where

$$f_{m,n,\xi,\alpha}(k,Q) = \frac{-2Im[\langle u_{n,\xi,\alpha}(k)\left|\frac{\partial H_\xi(k,Q)}{\partial k_x}\right|u_{m,\xi,\alpha}(k)\rangle\langle u_{m,\xi,\alpha}(k)\left|\frac{\partial H_\xi(k,Q)}{\partial k_y}\right|u_{n,\xi,\alpha}(k)\rangle]}{\{E_{n,\xi,\alpha}(k) - E_{m,\xi,\alpha}(k)\}^2} \tag{14}$$

The function $\Omega_{xy}^{(n)}(k)$ is the $z-$component of BC for the n^{th} occupied band $E_{n,\,\xi,\,\alpha}(k)$. BC is the analogue of the magnetic field in momentum-space while the Berry connection $\mathbf{A}_n(k)$ acts as a vector potential; that is, $\nabla_{\mathbf{k}} \times \mathbf{A}_{\mathbf{n}}(k) = \mathbf{\Omega}_{\mathbf{n}}(k)$. The Heisenberg equation of motion is $i\hbar(d\hat{x}/dt) = [\hat{x}, \hat{H}]$. In view of this equation, we find that the identity

$$\hbar\langle u_{n,\xi,\alpha}(\acute{k})|\hat{v}_J|u_{m,\xi,\alpha}(k)\rangle = (E_{n,\xi,\alpha}(\acute{k}) - E_{m,\xi,\alpha}(k))\langle u_{n,\xi,\alpha}(\acute{k})|\frac{\partial}{\partial k_j}|u_{m,\xi,\alpha}(k)\rangle$$

is satisfied for a system in a periodic potential and its Bloch states as the eigenstates $|u_{n,\xi,\alpha}(k)\rangle$. Here the operator $\hbar^{-1}\partial H_\xi(k,Q)/\partial k_j = \hat{v}_j$ represents the velocity in the $j = (x,\ y)$

direction. The $z-$component of BC may now be written in the form

$$\Omega_{x,y}(k) = -2\sum_n Im\left\langle \frac{\partial u_{n,\xi,\alpha}(k)}{\partial k_x} \middle| \frac{u_{n,\xi,\alpha}(k)}{\partial k_y} \right\rangle$$

upon using the identity above. We use this formula to calculate and represent BC (see also Appendix A 5) in Figure 6.

The 3D plots of the Berry curvature in the $z-$direction as a function of (ak_x, ak_y) around the HSP $T(0,\ 0,\ 0.2037)$ are shown in Figure 6. The numerical values of the parameters used are $P_0 = 0.32$, $P_1 = 2.71$, $M = 1$, $\mu = 0$, $Q = 0.86$, $v/a(v = v_F) = 0.50$, $\theta = 0$, $\eta_1 = 1$, and $\eta_2 = 0$. The tilt parameter $|\alpha_\xi| = 0.80$ (Figures 6(a)) and $|\alpha_\xi| = 2.8$ (Figures 6(b)). The Figures 6(c), and (d) correspond to the in-plane spin ordering as $\theta = \pi/2$. The rest of the parameter values in these figures are the same as in Figures 6(a), and (b). While in (c) tilt parameter is 0.9, in (d) tilt parameter is 1.14.

In order to investigate Berry-phase effect in anomalous thermoelectric transport, we will now consider the anomalous Nernst conductivity (ANC) $\alpha_{xy}(T)$. The conductivity needs to be computed by integrating the Berry curvatures close to the Fermi level along with the entropy density over first BZ [39], i.e.

$$\alpha_{xy}(\mu, T) = k_B \frac{e}{\hbar} \sum_{n,\xi=\pm1,\alpha=\pm1} \int d\mathbf{k} \Omega_{xy}^{(n)} s(E_{n,\xi,\alpha}(k))$$

where the entropy density $s(E_{n,\xi,\alpha}(k)$ is given by the expression

$$\begin{aligned} s(\varepsilon) &= \frac{\boldsymbol{\varepsilon} - \boldsymbol{\mu}}{k_B T} f(\boldsymbol{\varepsilon}) + \log\left(1 + \exp(\frac{\mu - \varepsilon}{k_B T})\right), \\ f(\boldsymbol{\varepsilon}) &= \frac{1}{1 + \exp(\frac{\varepsilon - \mu}{k_B T})} \end{aligned} \tag{15}$$

Here, $\boldsymbol{\mu}$ is the chemical potential, and $f(\boldsymbol{\varepsilon})$ is the Fermi-Dirac distribution with k_B the Boltzmann constant. In the low-temperature limit, upon using the Mott relation [40] we obtain

$$\alpha_{xy}(\mu) \approx \frac{\frac{\pi^2}{3} k_B^2 T}{e} \sum_{n,\xi=\pm1,\alpha=\pm1} \int d\mathbf{k} \Omega_{xy}^{(n)} \frac{\partial f(E_{n,\xi,\alpha(k)})}{\partial E_{n,\xi,\alpha(k)}}. \tag{16}$$

The 2D graphical representation of $\alpha_{xy}(T)$ as a function of $k_B T$ is shown in Figure 7. The plot shows that near $T = 0$, $\alpha_{xy}(T)$ assumes much larger value compared to those at higher temperature. The result is qualitatively same as that in Refs. [41, 42].

We conclude this section by noting that the Hall conductivity (σ_{xy}) is given by considering BC of all bands below the Fermi level $(E_F) : \sigma_{xy} = e^2/\hbar C$, and $C = 1/2\pi \sum_{E_n \le E_F} \int d\mathbf{k} \sigma_{xy}(k)$ where the integral is over the entire Brillouin zone (BZ) and corresponds to the sum of Berry curvatures of all occupied bands. It may also be noted that the Chern number is a property of a material and is particularly important because, being an integer, it cannot be

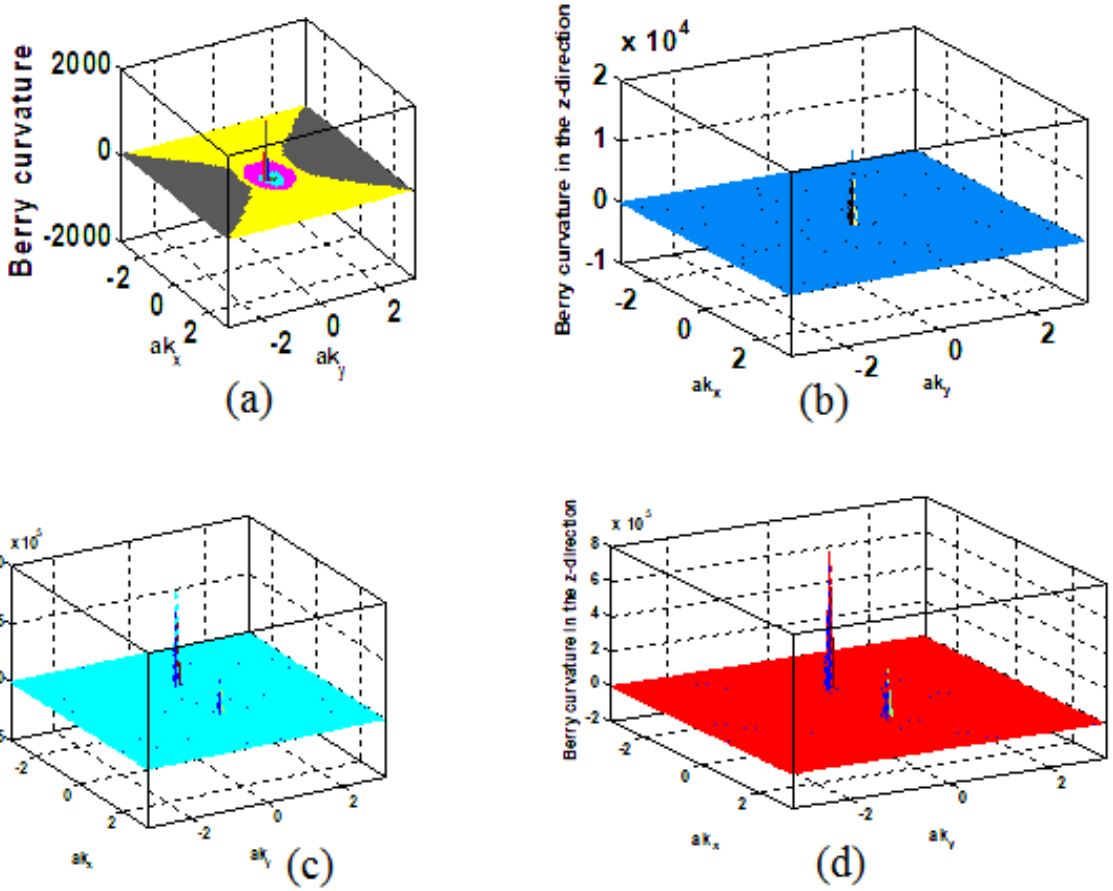

Figure 6. 3D plots of the Berry curvature in the $z-$direction as a function of $(ak_x,\ ak_y)$ around the HSP $T(0,\ 0,\ 0.2037)$. The numerical values of the parameters used are $P_0 = 0.32$, $P_1 = 2.71$, $M = 1$, $\mu = 0$, $Q = 0.86$, $v/a(v = v_F) = 0.50$, $\theta = 0$, $\eta_1 = 1$, and $\eta_2 = 0$. The angle $\theta = 0$ corresponds to the ferromagnetic order along the $z-$direction. The tilt parameter $|\alpha_\xi| = 0.80$ (Figures (a)) and $|\alpha_\xi| = 2.8$ (Figures (b)). The Figures 6(c), and (d) correspond to the in-plane spin ordering as $\theta = \pi/2$. The rest of the parameter values in these figures are the same as in Figures 6(a), and (b). (c) The tilt parameter 0.9. (d) The tilt parameteris 1.14.

changed under continuous deformations of the system. As shown in Figures 2(c), and (d) corresponding to the in-plane spin ordering ($\theta = \pi/2$), the system is an insulator with Fermi level (E_F) situated in the gap between the valence and the conduction band. In these cases the Chern number C, prima facie, is expected to have integer values. We, therefore, have calculated it in view of the fact that the in-plane spin ordering ($\theta = \pi/2$) on a 2D surface is embedded in the 3D system under consideration. It is usually difficult to exactly perform the integration of BC in order to seek the value of the Chern number. So, we are forced to rely on the Matlab package to obtain approximate value of C for the Figures 6(c), and (d). We make the problem of the integration manageable by breaking $k-$space into small grids and carry on with the integration. Our approximations gets better when we add more grids. We obtain $C \approx 2$ corresponding to both the figures with the appropriate choice of the parameter values and the number of grids. This indicates that, for the in-plane spin ordering ($\theta = \pi/2$), the anomalous Hall conductivity can be quantized topological phase with $C > 1$, though the system under consideration being three dimensional one.

5. Discussion with future perspective and conclusion

The recent observation of the ANE/AHE in $Co_3Sn_2S_2$ [43, 44], which boasts a kagome lattice, reinforces the significance of this compound. The magnetic kagome lattice's distinct symmetry and geometrical frustration foster an environment conducive to exotic topological states and anomalous transport phenomena, distinguishing it from other topological magnetic semimetals. Therefore, investigating the ANE and the AHE in $Co_3Sn_2S_2$ is crucial to understanding the origins of anomalous transport behaviors in MWSM systems. Furthermore, in ordinary metals the Sondheimer cancellation [45] typically renders the Nernst effect insignificant. Therefore, the importance of investigation of the anomalous contribution in magnetic Weyl semimetals becomes important. It has been already mentioned in section 4 that, whereas ANE is computed by the Berry curvature close to the Fermi level, the AHE is contributed from the sum of Berry curvatures of all occupied bands. The implication is that an insubstantial/substantial AHE does not necessarily imply an inconsiderable/considerable ANE due to differences in their underlying mechanisms. The observations above highlight the necessity of studying the ANE to underline the Berry curvature contribution.

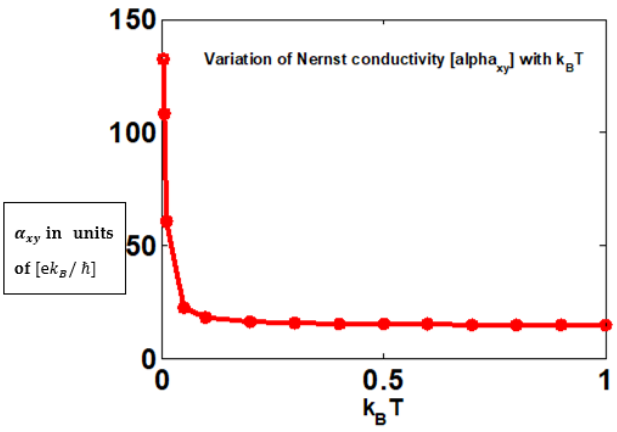

Figure 7. The plot of $\alpha_{xy}(T)$ as a function of k_BT for $\theta = 0$. The plot shows that near $T = 0$, $\alpha_{xy}(T)$ assumes much larger value compared to those at higher temperature. The numerical values of the parameters used are the same as those in Figure 6.

As mentioned in section 1 of this paper, Weyl fermions are massless, chiral quasiparticles with distinct spin polarization. In Weyl semimetals, opposing chiralities interact differently, resulting in chiral anomaly and bridging condensed matter and high-energy physics through relativistic field theory. The paper's principal findings are as follows: By employing the 2D SSH model (Eq. (5)), we incorporate the tilt of Weyl cones via the tilt velocity parameter, achieving substantial anomalous Nernst conductivity near $T = 0$. Importantly, for in-plane spin order ($\theta = \pi/2$) in a generic FMWSM featuring gapped energy spectra, we derive a Chern number $C \approx 2$, irrespective of the system's three-dimensional structure. The latter one is consistent with the Chern number's characterization of the non-trivial chiral charge associated with 3D Weyl points on an enclosing sphere. The explanation related to the surface Fermi arc formation, illustrated in Figure 1, is elaborated upon below.

The model (2) can be easily extended to a low-energy, minimalistic Hamiltonian for a two-band charge-n (positive integer) Weyl point or a multi-Weyl semimetal system. All that one needs to do is to replace the off-diagonal terms in (2) by $[(\xi\hbar v_F a^{-1})(aK_x \mp iaK_y)^n]$ where $aK_x = (ak_x - \xi eA_x)$ and $aK_y = (ak_y - \xi eA_y)$. In actual lattice systems, it is possible to consider $n = 1$, 2, and 3 [46, 47]. For example, one may consider the following two-band momentum space model for a charge-2 WSM

$$\begin{pmatrix} A(k_x,k_y,k_z) & C(k_x,k_y) - iDA(k_x,k_y) \\ C(k_x,k_y) + iDA(k_x,k_y) & B(k_x,k_y,k_z) \end{pmatrix}$$

with broken inversion, time-reversal and mirror symmetry, where $A = 2\Gamma(P - \cos k_x - \cos k_y - \cos k_z) + \beta\Gamma \sin k_z - \mu, B = -2\Gamma(P - \cos k_x - \cos k_y - \cos k_z) + \beta\Gamma \sin k_z - \mu, C = C = -2\Gamma(\cos k_x - \cos k_y)$, and $D = 2\Gamma(\sin k_x - \sin k_y)$, The numerical values of the parameters Γ, P, μ, etc. could be specified in conformity with Ref. [48]. This model has nodes at $(k_x, k_y, k_z) = (0, 0, \cos^{-1}(P - 2))$ for $1 \leq P \leq 3$. The calculation of anomalous Nernst conductivity could be carried out in the manner as above. As regards minimum lattice model of Charge-four weyl point and its chirality-dependent properties, one may refer to Ref. [49].

We have shown SFA in Figure 1. In order to explain this chirality preserving deformation of WNs we consider a minimalistic Hamiltonian (a variant of (2) without the tilt parameter) of the form $H_\xi(\mathbf{k}) = \xi v_F a^{-1}(\mathbf{k} - \xi e\mathbf{K}(z)), \boldsymbol{\sigma} + (\xi v_F a^{-1} k_z - \mu)\sigma_z$ where $\boldsymbol{\sigma} = (\sigma_x, \sigma_y)$, $\mathbf{k} + ()k_x, k_y$ and the vector potential $\mathbf{K} = e^{-1}(aK_x(z), aK_y(z))$. Obviously enough, one may define a pseudo-magnetic field here of the form $\mathbf{B}(z) = \nabla_{aK} \times \mathbf{K}(z)$. Upon Taylor expanding around a minimum $z_{0,n}$, the corresponding pseudo Landau levels are given by $E_n = \xi v_F a^{-1}(\mathbf{k} - \xi e\mathbf{K}(z_{0,n})) \cdot \hat{\mathbf{B}}$, where $\hat{\mathbf{B}}$ is a unit vector in the direction of $B(z)$. The pseudo-magnetic field may be interpreted as the one which stretches WNs into E_n. This is equivalent to SFA-an exotic non-closed surface state–shown in Figure 1 [50, 51].

As mentioned in the sub-section 2.2 above, the strain tensor $u_{ij} = 1/2(\partial_i u_j + \partial_j u_i)$, where u_j is the phonon vector field, can modify a pre-existing tilt making it inhomogeneous through the sample. In such a general case, the tilt velocity α_i in Hamiltonian (2) needs to be replaced by $\widetilde{\alpha}_l = \alpha_i + u_{ij}\alpha_j$. This issues will be investigated in future. Also, it will be shown that in the case of WSM the Kerr and ellipticity angles are substantially increased in comparison with those for an ordinary, non-topological metal in the absence of magnetic field. Furthermore, the FM materials with the out-of-plane magnetization has been the subject of numerous studies due to their applications in high-density magnetic recording and spintronic devices [52, 53]. The FM materials with in-plane magnetization has not been studied so extensively. This

is one of the main motivations to make a preliminary study of FM materials with the in-plane magnetization (see Figures 2(c, d), and Figures 6(c, d).

In this communication, we have alluded to the concepts of causation and the consorted event horizon in spacetime can be carried over into the field of Weyl materials, and thus depicting strong association [6] between condensed matter and high-energy physics. The causal structure of Weyl fermions is shown in Ref. [6], where the light cone resembles the Weyl cone, space to momentum, and time to energy. This issues will be investigated further in future.

In conclusion, the main motivation of the present work was to develop an understanding of WSMs from their effective low-energy theory. This is based on an interesting continuum model. We have investigated here anomalous Hall and Nernst conductivities which are related to BC. The longitudinal magnetoconductivity, the magneto-optical conductivity, and the magneto-thermal conductivity also bear the signature of BC. A systematic derivation of these quantities is left for future investigation. We finally note that WSMs possess many unusual optical properties such as they can exhibit BC related giant nonreciprocal effects. They may be used to construct ultra-compact optical isolators and circulators that are essential components in optical circuits.They generate high photogalvanic effect also which can potentially overcome the Shockley-Queisser limit of traditional solar cells.

Appendix A

$$|u_{\alpha,\xi}(k,Q)\rangle = \frac{1}{\sqrt{N_1(k,\xi,Q)}}\begin{pmatrix}\frac{\Upsilon_1(k)-i\Upsilon_2(k)}{E_{\alpha,\xi}(k)-\Upsilon(k)-A_0(k)}\\ 1\end{pmatrix}, \tag{17a}$$

$$N_1(k,\xi,Q) = 1+\frac{(\Upsilon_1(k))^2+(\Upsilon_2(k))^2}{\{E_{\alpha,\xi}(k)-\Upsilon(k)-A_0(k)\}^2}, \tag{17b}$$

$$\begin{aligned}\Upsilon_1(k) &= \xi v_F a^{-1}(ak_x)+\eta_1 M\sin\theta,\\ \Upsilon_2(k) &= \xi v_F a^{-1}(ak_y)+\eta_2 M\sin\theta,\end{aligned} \tag{17c}$$

$$A_0(k) = (P(\mathbf{k})+\xi\hbar v_F\frac{c}{a}k_z+M\cos\theta-\xi Q). \tag{17d}$$

$$\Upsilon(k) \equiv \xi v_F a^{-1}|\alpha_\xi|(ak_x\cos\psi+ck_z\sin\psi). \tag{17e}$$

We now consider the case where $|\alpha_\xi| = 0$. In this special case, the corresponding eigenvectors are given by

$$|u_{\alpha,\xi}(k,Q)\rangle = \frac{1}{\sqrt{N(k,\alpha,\xi,Q)}}\begin{pmatrix}\frac{\xi v_F aK_-}{\alpha[A_0(k)^2+(v_f aK)^2]^{1/2}-A_0(k)}\\ 1\end{pmatrix}, \tag{17f}$$

$$\xi v_F aK_\pm = (\xi v_F ak_\pm+\eta_1 M\sin\theta\pm i\eta_2 M\sin\theta), \tag{17g}$$

$$N(k,\alpha,\xi,Q) = 1+\frac{((v_F aK)^2}{\{\alpha[A_0^2(k)+(v_F aK)^2]^{1/2}-A_0(k)\}^2}, \tag{17h}$$

The eigenstates above are required for the calculation of BC. Upon using these states and the formula

$$\Omega_{xy}^{(n)}(k,\xi,\alpha) = -2Im\left\langle\frac{\partial u_{n,\xi,\alpha}(\mathrm{k})}{\partial k_x}\middle|\frac{\partial u_{n,\xi,\alpha}(\mathrm{k})}{\partial k_y}\right\rangle$$

we find that

$$\begin{aligned}\Omega_{xy}^{(n)}(k) &= \sum_{\xi=\pm1,\alpha=\pm1}\Omega_{xy}^{(n)}(k,\xi,\alpha) =\\ -2&\sum_{\xi=\pm1,\alpha=\pm1}(A_1(k)B_2(k)+A_2(k)B_1(k)),\end{aligned} \tag{17i}$$

$$\begin{aligned}A_1(k) = -\frac{1}{2N_1^{3/2}}&\frac{\partial N_1(\mathrm{k})}{\partial k_x}\frac{\Upsilon_1(k)}{\{E_{\alpha,\xi}(k)-\Upsilon(k)-A_0(k)\}}+\\ &\frac{\frac{\partial\Upsilon_1(k)}{\partial k_x}N_1^{-1/2}}{\{E_{\alpha,\xi}(k)-\Upsilon(k)-A_0(k)\}}-\frac{N_1^{-1/2}\Upsilon_1(k)\frac{\partial E_0(k,\alpha,\xi)}{\partial k_x}}{\{E_{\alpha,\xi}(k)-\Upsilon(k)-A_0(k)\}^2},\end{aligned} \tag{17j}$$

$$\begin{aligned}B_1(k) = -\frac{1}{2N_1^{3/2}}&\frac{\partial N_1(K)}{\partial k_x}\frac{\Upsilon_2(k)}{\{E_{\alpha,\xi}(k)-\Upsilon(k)-A_0(k)\}}+\\ &\frac{\frac{\partial\Upsilon_2(k)}{\partial k_x}N_1^{-1/2}}{\{E_{\alpha,\xi}(k)-\Upsilon(k)-A_0(k)\}}-\frac{N_1^{-1/2}\Upsilon_2(k)\frac{\partial E_0(k,\alpha,\xi)}{\partial k_x}}{\{E_{\alpha,\xi}(k)-\Upsilon(k)-A_0(k)\}^2},\end{aligned} \tag{17k}$$

$$\begin{aligned}A_2(k) = -\frac{1}{2N_1^{3/2}}&\frac{\partial N_1(\mathrm{k})}{\partial k_y}\frac{\Upsilon_1(k)}{\{E_{\alpha,\xi}(k)-\Upsilon(k)-A_0(k)\}}+\\ &\frac{\frac{\partial\Upsilon_1(k)}{\partial k_y}N_1^{-1/2}}{\{E_{\alpha,\xi}(k)-\Upsilon(k)-A_0(k)\}}-\frac{N_1^{-1/2}\Upsilon_1(k)\frac{\partial E_0(k,\alpha,\xi)}{\partial k_y}}{\{E_{\alpha,\xi}(k)-\Upsilon(k)-A_0(k)\}^2},\end{aligned} \tag{17l}$$

$$\begin{aligned}B_2(k) = \frac{1}{2N_1^{3/2}}&\frac{\partial N_1(K)}{\partial k_y}\frac{\Upsilon_2(k)}{\{E_{\alpha,\xi}(k)-\Upsilon(k)-A_0(k)\}}+\\ &\frac{\frac{\partial\Upsilon_2(k)}{\partial k_y}N_1^{-1/2}}{\{E_{\alpha,\xi}(k)-\Upsilon(k)-A_0(k)\}}-\frac{N_1^{-1/2}\Upsilon_2(k)\frac{\partial E_0(k,\alpha,\xi)}{\partial k_y}}{\{E_{\alpha,\xi}(k)-\Upsilon(k)-A_0(k)\}^2},\end{aligned} \tag{17m}$$

$$E_0(k,\alpha,\xi) = \{E_{\alpha,\xi}(k)-\Upsilon(k)-A_0(k)\} \tag{17n}$$

Equations 17a-17n have been used to obtain the graphical representations of BC in Figure 6.

Authors contributions

U. P. Tyagi and P. Goswami are the authors of this manuscript and have contributed equally.

Availability of data and materials

No data was used for the research described in the article.

Conflict of interests

The author declare that they have no known competing financial interests or personal relationships that could have appeared to influence the work reported in this paper.

References

[1] S.Jia, M. Z. Hasan, et al. "Weyl semimetals, Fermi arcs and chiral anomalies.". *Nature Mater*, **15**:1140, 2016. DOI: https://doi.org/10.1038/nmat4787.

[2] Q. Ma, S. Y. Xu, et al. "Direct optical detection of Weyl fermion chirality in a topological semimetal. ". *Nature Phys*, **13**:842–847, 2017. DOI: https://doi.org/10.1038/nphys4146.

[3] J. Bell and R. Jackiw. "A PCAC puzzle: $\pi^0 \to \gamma\gamma$ in the σ-model. ". *Nuovo Cimento A*, **60**:47, 1969. DOI: https://doi.org/10.1007/BF02823296.

[4] K. Landsteiner. "Notes on anomaly induced transport. ". *Acta Physica Polonica B*, **47**:2617, 2016. DOI: https://doi.org/10.5506/APhysPolB.47.2617.

[5] S. L. Adler. "Axial-Vector Vertex in Spinor Electrodynamics. ". *Phys. Rev.*, **177**:426, 1969. DOI: https://doi.org/10.1103/PhysRev.177.2426.

[6] W. C. Chiu, G. Chang, G. Macam, et al. "Causal structure of interacting Weyl fermions in condensed matter systems. ". *Nat Commun*, **14**:2228, 2023. DOI: https://doi.org/10.1038/s41467-023-37931-w.

[7] D. Liu, A. Liang, E. Liu, Q. Xu, et al. "Magnetic Weyl semimetal phase in a Kagomé crystal. ". *Science*, **365**:1282, 2019. DOI: https://doi.org/10.1126/science.aav2873.

[8] L. Yang, Z. Liu, Y. Sun, H. Peng, et al. "Weyl semimetal phase in the non-centrosymmetric compound TaAs.". *Nature Physics*, **11**:728, 2015. DOI: https://doi.org/10.1038/nphys3425.

[9] H. Weng, C. Fang, Z. Fang, B. A. Bernevig, and X. Dai. "Weyl semimetal phase in noncentrosymmetric transition-metal monophosphides. ". *Phys. Rev. X*, **5**:011029, 2015. DOI: https://doi.org/10.1103/PhysRevX.5.011029.

[10] S.-M. Huang, S.-Y. Xu, I. Belopolski, et al. "A Weyl Fermion semimetal with surface Fermi arcs in the transition metal monopnictide TaAs class. ". *Nature communications*, **6**:7373, 2015. DOI: https://doi.org/10.1038/ncomms8373.

[11] C. L. Zhang, S. Y. Xu, I. Belopolski, et al. "Signatures of the Adler–Bell–Jackiw chiral anomaly in a Weyl fermion semimetal. ". *Nat Commun*, **7**:10735, 2016. DOI: https://doi.org/10.1038/ncomms10735.

[12] N. Xu, H. Weng, B. Lv, C. E. Matt, et al. "Observation of Weyl nodes and Fermi arcs in tantalum phosphide. ". *Nature communications*, **7**:11006, 2016. DOI: https://doi.org/10.1038/ncomms11006.

[13] P. Li, Y. Wen, X. He, et al. "Evidence for topological type-II Weyl semimetal WTe_2. ". *Nat Commun*, **8**:2150, 2017. DOI: https://doi.org/10.1038/s41467-017-02237-1.

[14] E. Liu, Y. Sun, N. Kumar, L. Müchler, et al. "Giant anomalous Hall effect in a ferromagnetic Kagomé-lattice semimetal. ". *Nat. Phys.*, **14**:1125–1131, 2018. DOI: https://doi.org/10.1038/s41567-018-0234-5.

[15] L. Ye, M. Kang snd J. Liu, et al. "Massive Dirac fermions in a ferromagnetic kagome metal.". *Nature*, **555**:638, 2018. DOI: https://doi.org/10.1038/nature25987.

[16] A. Ozawa and K. Nomura. "Two-Orbital effective model for magnetic Weyl semimetal in Kagome-Lattice Shandite. ". *Journal of the Physical Society of Japan*, **88**:123703, 2019. DOI: https://doi.org/10. 7566/JPSJ.88.123703.

[17] N. Morali and R. Batabyal. "Fermi-arc diversity on surface terminations of the magnetic Weyl semimetal $Co_3Sn_2S_2$. ". *Science*, **365**:1286, 2019. DOI: https://doi.org/10.1126/science.aav2334.

[18] S. N. Guin, J. Gooth, et al. "Zero-Field Nernst effect in a ferromagnetic Kagome-Lattice Weyl-semimetal $Co_3Sn_2S_2$.". *Adv. Mater.*, **31**:e1806622, 2019. DOI: https://doi.org/10.1002/adma.201806622.

[19] D. F. Liu, A. J. Liang, et al. "Magnetic Weyl semimetal phase in a Kagomé crystal. ". *Science*, **365**:1282, 2019. DOI: https://doi.org/10.1126/science.aav2873.

[20] S. Howard, L. Jiao, Z. Wang, N. Morali, R. Batabyal, et al. "Evidence for one-dimensional chiral edge states in a magnetic Weyl semimetal $Co_3Sn_2S_2$. ". *Nature Communications*, **12**:4269, 2021. DOI: https://doi.org/10.1038/s41467-021-24561-3.

[21] A. Ozawa and K. Nomura. "Self-consistent analysis of doping effect for magnetic ordering in stacked-kagome Weyl system.". *Phys.Rev.Materials*, **6**:024202, 2022. DOI: https://doi.org/10.1103/PhysRevMaterials.6.024202.

[22] I. Belopolski, K. Manna, D. S. Sanchez, G. Chang, B. Ernst, et al. "Discovery of topological Weyl fermion lines and drumhead surface states in a room temperature magnet. ". *Science*, **365**:1278, 2019. DOI: https://doi.org/10.1126/science.aav2327.

[23] I. Belopolski, S.-Y. Xu, et al. "Criteria for directly detecting topological Fermi Arcs in Weyl semimetals.". *Phys. Rev. Lett.*, **116**:066802, 2016. DOI: https://doi.org/10.1103/PhysRevLett.116.066802.

[24] S.-Y. Xu, I. Belopolski, et al. "Spin polarization and texture of the Fermi Arcs in the Weyl Fermion semimetal TaAs. ". *Phys. Rev. Lett.*, **116**:096801, 2016. DOI: https://doi.org/10.1103/PhysRevLett.116.096801.

[25] S. Nandy, C. Lane, and J.-X. Zhu. "Quantum Hall effect in a Weyl-Hubbard model:Interplay between topology and correlation. ". *Phys. Rev. B*, **109**:085111, 2024. DOI: https://doi.org/10.1103/PhysRevB.109.085111.

[26] H. B. Nielsen and M. Ninomiya. "A no-go theorem for regularizing chiral fermions. ". *Phys. Lett. B*, **105**:219, 1981. DOI: https://doi.org/10.1016/0370-2693(81)91026-1.

[27] Z. Ren, H. Li, S. Sharma, et al. "Plethora of tunable Weyl fermions in kagome magnet Fe_3Sn_2 thin films. ". *npj Quantum Mater.*, **7**:109, 2022. DOI: https://doi.org/10.1038/s41535-022-00521-y.

[28] M. Z. Hasan et al. "Weyl, Dirac and high-fold chiral fermions in topological quantum matter.". *Nat. Rev. Mater.*, **6**:784–803, 2021. DOI: https://doi.org/10.1038/s41578-021-00301-3.

[29] S. Fang et al. "Ferromagnetic helical nodal line and Kane-Mele spin-orbit coupling in kagome metal Fe_3Sn_2. ". *Phys. Rev. B*, **105**:035107, 2022. DOI: https://doi.org/10.1103/PhysRevB.105.035107.

[30] J. Gooth, B. Bradlyn, et al. "Axionic charge-density wave in the Weyl semimetal (TaSe4)2I. ". *Nature*, **575**:315, 2019. DOI: https://doi.org/10.1038/s41586-019-1630-4.

[31] S. Nie, T. Hashimoto, and F. B. Prinz. "Magnetic Weyl Semimetal in $K_2Mn_3(AsO_4)_3$ with the Minimum Number of Weyl Points.". *Phys. Rev. Lett.*, **128**:176401, 2022. DOI: https://doi.org/10.1103/PhysRevLett.128.176401.

[32] X. Feng, K.Ziang, et al. "Chiral flux phase in the Kagome superconductor AV_3Sb_5.". *Sci.Bull.*, **66**:1384, 2021. DOI: https://doi.org/10.1016/j.scib.2021.04.043.

[33] H.-S. Xu, Y.-J Yan, et al. "Multiband superconductivity with sign-preserving order parameter in Kagome superconductor CsV_3Sb_5. ". *Phys.Rev.Lett.*, **127**:187004, 2021. DOI: https://doi.org/10.1103/PhysRevLett.127.187004.

[34] W. Zhang, X. Liu, et al. "Nodeless superconductivity in Kagome metal CsV_3Sb_5 with and without time reversal symmetry breaking. ". *Nano Lett.*, **23**:872, 2023. DOI: https://doi.org/10.1021/acs.nanolett.2c04103.

[35] E. Liu, Y. Sun, et al. "Giant anomalous Hall effect in a ferromagnetic kagome-lattice semimetal. ". *Nat. Phys.*, **14**: 1125, 2018. DOI: https://doi.org/10.1038/s41567-018-0234-5.

[36] C. L. Kane and E. J. Mele. "Quantum spin Hall effect in graphene. ". *Phys. Rev. Lett.*, **95**:226801, 2005. DOI: https://doi.org/10.1103/PhysRevLett.95.226801.

[37] F. D. M. Haldane. "Berry curvature on the Fermi Surface: Anomalous Hall effect as a topological Fermi-Liquid property. ". *Phys. Rev. Lett.*, **93**:206602, 2004. DOI: https://doi.org/10.1103/PhysRevLett.93.206602.

[38] M. Chen and S. Wan. "The quantum anomalous Hall effect on a star lattice with spin–orbit coupling and an exchange field.". *J. Phys.: Condens. Matter*, **24**:325502, 2012. DOI: https://doi.org/10.1088/0953-8984/24/32/325502.

[39] D. Xiao, M.-C. Chang, and Q. Niu. "Berry phase effects on electronic properties. ". *Rev. Mod. Phys.*, **82**:1959–2007, 2010. DOI: https://doi.org/10.1103/RevModPhys.82.1959.

[40] D. Xiao, Y. Yao, Z. Fang, and Q. Niu. "Berry phase effect in anomalous thermoelectric properties. ". *Phys.Rev. Lett.*, **97**:026603, 2006. DOI: https://doi.org/10.1103/PhysRevLett.97.026603.

[41] M. Ikhlas, T. Tomita, et al. "Large anomalous Nernst effect at room temperature in a chiral antiferromagnet.". *Nat. Phys.*, **13**:1085, 2017. DOI: https://doi.org/10.1038/nphys4181.

[42] P. Goswami and S. Tewari. "Axionic field theory of $(3+1)$-dimensional Weyl semimetals.". *Phys. Rev. B*, **88**:245107, 2013. DOI: https://doi.org/10.1103/PhysRevB.88.245107.

[43] H. Yang, W. You, et al. "Giant anomalous Nernst effect in the magnetic Weyl semimetal $Co_3Sn_2S_2$.". *Phys. Rev. Materials*, **4**:024202, 2020. DOI: https://doi.org/10.1103/PhysRevMaterials.4.024202.

[44] E. K. Liu, Y. Sun, et al. "Giant anomalous Hall effect in a ferromagnetic Kagomé-lattice semimetal.". *Nat. Phys.*, **14**: 1125, 2018. DOI: https://doi.org/10.1038/s41567-018-0234-5.

[45] E. H. Sondheimer. "The theory of the galvanomagnetic and thermomagnetic effects in metals. ". *Proc. R. Soc. London, Ser. A*, **193**:484, 1948. DOI: https://doi.org/10.1098/rspa.1948.0058.

[46] T. Zhang, R. Takahashi, et al. "Twofold quadruple Weyl nodes in chiral cubic crystals. ". *Phys. Rev. B*, **102**:125148, 2020. DOI: https://doi.org/10.1103/PhysRevB.102.125148.

[47] Z.-M. Yu, Z. Zhang, et al. "Encyclopedia of emergent particles in three-dimensional crystals. ". *J. Comput. Phys.*, **67**: 375, 2022. DOI: https://doi.org/10.1016/j.scib.2021.10.023.

[48] B. Singh, G. Chang, et al. "Tunable double-Weyl Fermion semimetal state in the $SrSi_2$ materials class. ". *Scientific Reports*, **8**:10540, 2018. DOI: https://doi.org/10.1038/s41598-018-28644-y.

[49] C. Cui, X.-P. Li, et al. "Charge-four Weyl point: Minimum lattice model and chirality-dependent properties. ". *Phys. Rev. B*, **104**:075115, 2021. DOI: https://doi.org/10.1103/PhysRevB.104.075115.

[50] A. G. Grushin, J. W. F. Venderbos, et al. "Inhomogeneous Weyl and Dirac semimetals: Transport in Axial magnetic fields and Fermi Arc surface states from Pseudo-Landau levels. ". *Phys. Rev. X*, **6**:041046, 2016. DOI: https://doi.org/10.1103/PhysRevX.6.041046.

[51] H. Zhang et al. "Giant periodic pseudomagnetic fields in strained Kagome magnet FeSn Epitaxial films on $SrTiO_3(111)$ substrate.". *Nano Lett.*, **13**:2397, 2023. DOI: https://doi.org/10.1021/acs.nanolett.3c00345.

[52] N. P. Armitage, E. J. Mele, et al. "Weyl and Dirac semimetals in three-dimensional solids. ". *Rev. Mod. Phys.*, **90**:015001, 2018. DOI: https://doi.org/10.1103/RevModPhys.90.015001.

[53] R. Ilan, A. G. Grushin, and D. I. Pikulin. "Pseudo-electromagnetic fields in 3D topological semimetals. ". *Nat. Rev.Phys.*, **2**:29, 2020. DOI: https://doi.org/10.1038/s42254-019-0121-8.